



Nanoscale

**Observing the Colloidal Stability of Iron Oxide Nanoparticles  
*in situ***

Journal:	<i>Nanoscale</i>
Manuscript ID	NR-ART-04-2019-003709
Article Type:	Paper
Date Submitted by the Author:	30-Apr-2019
Complete List of Authors:	Hufschmid, Ryan; University of Washington, Materials Science & Engineering Teeman, Eric; University of Washington, Materials Science and Engineering Mehdi, Layla; University of Liverpool Krishnan, Kannan; University of Washington, Materials Science Browning, Nigel ; University of Liverpool, Department of Mechanical, Materials and Aerospace Engineering; University of Liverpool, Department of Physics; Pacific Northwest National Laboratory, Physical and Computational Science Directorate

SCHOLARONE™  
Manuscripts

# Observing the Colloidal Stability of Iron Oxide Nanoparticles *in situ*

Ryan Hufschmid,<sup>1\*</sup> Eric Teeman,<sup>1</sup> B. Layla Mehdi,<sup>2,3</sup>  
Kannan M. Krishnan,<sup>1§</sup> and Nigel D. Browning<sup>2,3,4†</sup>

<sup>1</sup>Department of Materials Science & Engineering, University of Washington, Seattle, WA  
98195-2129, USA

<sup>2</sup>Department of Mechanical, Materials and Aerospace Engineering, University of Liverpool,  
Liverpool L69 3GH, UK

<sup>3</sup>Department of Physics, University of Liverpool, Liverpool L69 3GH, UK

<sup>4</sup>Physical and Computational Science Directorate, Pacific Northwest National Laboratory,  
Richland, WA 99352, USA

\*rhuf@uw.edu §kannanmk@uw.edu †nigel.browning@liverpool.ac.uk

## Abstract

Colloidal processes such as nucleation, growth, ripening, and dissolution are fundamental to the synthesis and application of engineered nanoparticles, as well as numerous natural systems. In nanocolloids consisting of a dispersion of nanoparticles in solution, colloidal stability is influenced by factors including particle surface facet and capping layer, and local temperature, chemistry, and acidity. In this paper, we investigate colloidal stability through the real-time manipulation of nanoparticles using *in situ* liquid cell Scanning Transmission Electron Microscopy (STEM). In a distribution of uniform iron oxide nanoparticles, we use the electron beam to precisely control the local chemistry of the solution and observe the critical role that surface chemistry plays in nanoparticle stability. By functionalizing the nanoparticle surfaces with charged amino acids and peptides, stability can be tuned to promote dissolution, growth, or agglomeration, either permanently or reversibly. STEM imaging is used to quantify kinetics of individual nanoparticles subject to local variations in chemistry. These measurements of dissolution and growth rates of iron oxide nanoparticles provide insights into nanoparticle stability relevant to synthesis and functionalization for biomedical applications.

## Introduction

Nanoscale colloidal processes such as nucleation, growth, dissolution, and self-assembly govern many environmental and biological systems.<sup>1,2,3</sup> A diverse set of important technologies also depend on the properties of colloidal nanoparticles, from catalysis<sup>4,5</sup> and energy storage<sup>6</sup> to medical applications.<sup>7-9</sup> For targeted applications of nanoparticles, it is critical to understand how colloidal stability is determined by the dynamics of the solid-liquid interface. This is particularly important at the interface of nanoparticles with complex biological systems, where safety and efficacy of therapeutics depend on our understanding of these phenomena.<sup>10-13</sup> Iron oxide nanoparticles (IONPs) are one prominent example, with a wide variety of biomedical imaging and therapeutic applications.<sup>8,9</sup> Iron oxides are prevalent in nature, generally non-toxic, and inexpensive to synthesize.<sup>14-17</sup> These benefits, combined with their magnetic properties, make IONPs a superb platform for many engineered biomedical applications. IONP stability depends on their environment—inside biological cells interactions between nanoparticles and the cellular solution affects their rotational dynamics and magnetic performance.<sup>18</sup> Further, IONPs accumulate in lysosomes, which break down foreign objects in part by dissolving them in their acidic enzymatic environment.<sup>19-22</sup> While IONPs may be functionalized with various chemical species for targeting or other functionality,<sup>23-25</sup> this modification affects the nanoparticle surface chemistry and charge, mediating interactions with ions or other species in solution, and affecting their stability.<sup>26-29</sup>

The solid-liquid interface is often considered an electric double layer (EDL)—an inner layer of strongly adsorbed solvent ions forms at the surface, while further away from the particle, in the Stern and diffuse layers, loosely associated ions move under the influence of Coulombic forces and Brownian motion.<sup>30-32</sup> To quantify surface charge, the zeta potential ( $\zeta$ ) is defined as

the electric potential, relative to the bulk solution, at the slipping plane of the solid-liquid interface. While convenient to measure experimentally by dynamic light scattering (DLS),  $\zeta$  does not directly describe conditions within the EDL or the Stern layer where ion exchange, adsorption, and other interfacial phenomena occur. Furthermore, the classical EDL model does not provide an analytical description for spherical particles or in ionic liquids.<sup>33</sup> The effect of surface charge on colloidal stability depends on the solution—in high ion content solutions surface charge will cause aggregation, while the same surface charge in DI water will be a stabilizing factor. Steric bulk of surface molecules is another stabilizing mechanism important for biological applications or other environments with high ionic and molecular content.<sup>7,10</sup> Recent investigations of solid-liquid interfaces have relied on a combination of molecular dynamic simulations,<sup>34–37</sup> and experimental observation with scanning probe techniques.<sup>2,33,38</sup> Understanding the interfacial kinetics behind colloidal stability ultimately requires the development of techniques capable of direct, real-time observation. In this work, we directly observe IONPs *in situ*, with liquid cell Scanning Transmission Electron Microscopy (STEM), to quantify how surface chemistry and solution conditions affect the colloidal stability of individual and ensembles of nanoparticles.

A modern TEM is a powerful tool for characterizing structure and chemistry at the nanoscale, with direct detectors and dynamic pulsed TEMs pushing temporal resolution to the timescales necessary to study many chemical reactions.<sup>39,40</sup> *In situ* techniques aim to simulate relevant environmental conditions, e.g. liquids,<sup>41–44</sup> gasses,<sup>45,46</sup> or external stimuli,<sup>39,47</sup> inside the TEM column. While *in situ* methodologies have been applied nearly as long as TEM,<sup>48</sup> recent development of specialized holders and instruments have made *in situ* experiments more practical. Liquid TEM in particular enables observation of nanoparticle growth and stability,<sup>49–52</sup> oriented attachment,<sup>36</sup> and electrochemistry,<sup>53–55</sup> providing unique insight into the nature of the solid-liquid

interface. Imaging with TEM exposes the sample to high-energy electrons, which can initiate secondary reactions or phase changes such as nucleation, growth, or dissolution.<sup>49-51</sup> The dependence of the stability of gold nanoparticles on pH and electron dose has been shown with *in situ* TEM.<sup>52</sup> TEM irradiation of water decreases the solution pH as a function of electron flux density.<sup>50,56</sup> The acidic pH under electron irradiation can be used to induce nanoparticle transformations in conditions analogous to other acidic aqueous conditions.

## Experimental Methods

Magnetite ( $\text{Fe}_3\text{O}_4$ ) IONP cores were synthesized by organic thermal decomposition of iron(III) oleate in 1-octadecene and oleic acid.<sup>57,58</sup> A single batch of particles with low size dispersity was selected for surface coating. As-synthesized oleic acid terminated IONPs were transferred to aqueous phase by coating with a copolymer of poly(maleic anhydride-*alt*-1-octadecene) and poly(ethylene glycol) (PMAO-PEG).<sup>59,60</sup> The exposed terminal end of PEG included a maleimide functional group to provide a platform for further surface functionalization. An arginine-rich cell penetrating peptide (CPP) and the amino acid L-cysteine were conjugated to PEG coated IONPs through sulfhydryl-maleimide coupling at neutral pH. Conjugated IONPs were purified by two cycles of centrifugation/filtration using a membrane filtration device (Millipore) containing a 30 kDa molecular weight cutoff to remove excess polymer. The final suspension of IONPs was diluted with deionized water to a concentration of  $1 \text{ mgFe}_3\text{O}_4 \text{ mL}^{-1}$ .

TEM experiments are performed on an FEI Titan 80-300<sup>TM</sup> STEM operated in scanning mode, in which the focused and aberration corrected probe is rastered across the specimen. Scattered electrons are collected on a Gatan High-Angle Annular Dark Field (HAADF) detector to generate an image of the specimen with contrast approximately proportional to mass-

thickness.<sup>61</sup> Liquid cells are assembled in a Hummingbird liquid stage, with closed cell (no flow) and chips with 50 nm thick SiN<sub>x</sub> windows. The inside SiN<sub>x</sub> window is treated with a 30 sec O<sub>2</sub>/Ar plasma. Then 0.2 μL of the IONP solution is pipetted onto the (upside-down) upper chip and the lower chip is placed on top. The entire cell is sealed in the holder which rotates during loading into the microscope so that the upper chip is now on top. The solution and microscope vacuum cause the window to bulge. Fluid thickness, determined with Electron Energy Loss Spectroscopy (EELS), is 100-200 nm near the window edge where these experiments are performed (See Supplementary Information). The STEM probe current is calibrated with a Faraday cup sample holder; the electron flux density ( $e^- \text{Å}^{-2} \text{s}^{-1}$ ), sometimes referred to as “dose rate,” is calculated by multiplying the current by the frame time, including flyback time.<sup>44</sup> For these experiments the calibrated probe current is approximately 10 pA at the specimen plane, except when noted otherwise, and electron flux density is controlled by increasing STEM magnification to scan the probe over a smaller area.

## Results

To understand the effect of surface chemistry on colloidal stability, IONPs with three different surface coatings are prepared for *in situ* imaging. IONPs with hydrophobic capping ligands synthesized in organic solvents are coated with an amphiphilic polymer to stabilize in aqueous solutions.<sup>57,62,60</sup> Here we use a (PMAO-PEG) for aqueous phase transfer. First, methoxy terminated, PEG coated (Methoxy-PEG) IONPs are studied to establish the behavior of uniform IONPs in water under electron irradiation in the TEM. Second, particles functionalized with the amino acid L-cysteine (L-Cys-PEG) and third, an arginine-rich cell-penetrating peptide (CPP-PEG) are characterized to investigate the role of surface chemistry on interactions in solution.

Average core diameter ( $d_C$ ) and lognormal size distribution ( $\sigma$ ) are fit to Vibrating Sample Magnetometry (VSM) measurements,<sup>63</sup> and confirmed with TEM. **Figure 1** is a representative STEM image of the IONP cores. The zeta potential ( $\zeta$ ) and hydrodynamic size ( $d_H$ ) are measured by Dynamic Light Scattering (DLS) for the three different surface coatings at room temperature in DI water. These physio-chemical properties are summarized in **Table 1**.

Previous works have measured the pH dependence of the zeta potential for IONPs functionalized with, for example, chitosan<sup>24</sup> or peptide dendrimers.<sup>25</sup> The pH behavior of functionalized IONPs is typical of colloidal systems:  $\zeta$  is negative and stabilized at basic pH, and as pH is decreased  $\zeta$  passes through the isoelectric point before approaching a positive  $\zeta$  at an acidic pH. As the solution becomes more acidic, the zeta potential increases and positive ions, including iron  $2^+/3^+$ , are driven into the Stern layer. Increasing the local iron concentration increases the stability of solid phases and may produce supersaturation, prompting growth of iron oxide phases (see Supplemental Information).

Methoxy-PEG coated IONPs dissolve with time and dose when observed in a liquid cell in the TEM, as shown in **Figure 2a-c** and Supplementary Movie 1. The dissolution is dependent on the electron flux density, with particle size (diameter) decreasing with accumulated dose (**Figure 2d**). Increasing the magnification, and thus the flux density, increases the rate of dissolution from  $0.02 \text{ nm s}^{-1}$  at  $0.8 \text{ e}^- \text{ \AA}^{-2} \text{ s}^{-1}$  to  $0.10 \text{ nm s}^{-1}$  at  $6.6 \text{ e}^- \text{ \AA}^{-2} \text{ s}^{-1}$  to  $0.19 \text{ nm s}^{-1}$  at  $24.8 \text{ e}^- \text{ \AA}^{-2} \text{ s}^{-1}$ . For Methoxy-PEG coated  $\text{Fe}_3\text{O}_4$ , we do not observe a threshold dose below which particles are stable. Even under relatively low dose conditions ( $< 1 \text{ e}^- \text{ \AA}^{-2} \text{ s}^{-1}$ ) dissolution is apparent within several minutes.

To observe the effect of the surface chemistry on stability, we next observe the PMAO-PEG coated particle functionalized with the amino acid L-cysteine. L-cysteine is zwitterionic, with

both positive and negative charge. L-Cys-PEG particles grow when electron flux density is greater than  $5 \text{ e}^- \text{ \AA}^{-2} \text{ s}^{-1}$ , as iron is driven from the iron oxide core into the surface coating. When the flux density is reduced back to  $1 \text{ e}^- \text{ \AA}^{-2} \text{ s}^{-1}$ , by decreasing the magnification, the surface layer dissolves. This reversible growth is shown in the time series in **Figure 3**, and in **Supplementary Movie 2**. In the experiment, one particle was imaged at high magnification and irradiated with sufficient electron flux to promote dissolution and recrystallization. Growth occurs in the polymer layer (not visible) that extends an additional  $\sim 30 \text{ nm}$  from the particle surface. Even after three cycles of growth and dissolution, we still see a gap around the initial particle core indicating that the polymer coating is still intact and strongly interacting with the particle surface, and the performance of the polymer coating has not been permanently changed. However, the growth kinetics do change between cycles: for the first cycle, the iron oxide interface moves at approximately  $0.2 \text{ nm s}^{-1}$ , while growth during second and third cycle increases to  $0.4 \text{ nm s}^{-1}$ . This indicates that some iron remains in the coating, increasing the rate of recrystallization on subsequent runs.

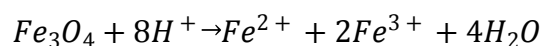
Imaging contrast in high-angle annular dark field (HAADF) STEM is proportional to atomic number.<sup>61,64</sup> Iron thus scatters more strongly due to its significantly higher atomic number than atoms in the polymer coating. Accumulation of iron at the particle surface appears as increased contrast in the images. In this way we can quantify growth of the particle by integrating the radial intensity of the HAADF detector, as shown in **Figure 3**. Post-mortem EDS and EELS analyses also confirm the presence of iron in the surface growths (see Supplementary Information).

Unlike the reaction facilitated by L-Cys-PEG, growth of CPP-PEG functionalized IONPs is not reversible. When these particles are imaged in the STEM liquid cell, at low doses (electron flux density  $< 1 \text{ e}^- \text{ \AA}^{-2} \text{ s}^{-1}$ ) we do not observe any growth. At a flux density of  $1.3 \text{ e}^- \text{ \AA}^{-2} \text{ s}^{-1}$ , the particles grow as iron diffuses out of primary particles, shown for an ensemble of IONPs in **Figure**

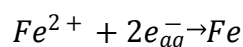
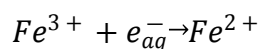
5. No growth species, *i.e.* iron, are added to solution so the solid phases precipitate from previously dissolved particles elsewhere in solution. In **Figure 5**, dissolving particles are circled. When the CPP-PEG particles were left with the beam off for 20 min, they recrystallized, forming a disordered hydrated iron oxide phase shown in **Figure 5c**. When the flux density is increased to  $14.1 \text{ e}^- \text{ \AA}^{-2} \text{ s}^{-1}$ , these CPP-PEG particles dissolve. We expect IONPs in aqueous environments will typically dissolve under a moderate electron flux of  $10\text{-}100 \text{ e}^- \text{ \AA}^{-2} \text{ s}^{-1}$ , regardless of the surface coating.

## Discussion

Iron oxides will dissolve in aqueous environments, facilitated by excess hydrogen ions:

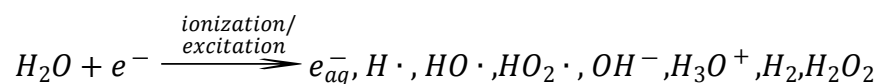


In acidic solutions,  $\text{Fe}^{2+}$  is the favored equilibrium product, as indicated by the Pourbaix diagram (see Supplementary Information). If reductive species are present, represented below as aqueous electrons, further reduction of iron is possible.



Small perturbations of the local conditions, e.g. pH, caused even by relatively low doses of electrons ( $<1 \text{ e}^- \text{ \AA}^{-2} \text{ s}^{-1}$ ) can induce dynamic and unexpected phase transformations. *In situ* electron microscopy inherently involves interaction between high-energy electrons and the sample.<sup>42,44,50,56</sup> The electron flux density and total dose are monitored and kept below damage thresholds. But if electron-specimen interactions are not considered, beam damage can confuse interpretation. This reinforces the importance of understanding, measuring, and reporting *in situ* TEM conditions. An important consequence of electron-water interactions is the production of

reactive species in solution, namely  $H^+$  and aqueous electrons, as a function of dose.<sup>50,56</sup> For deionized water ( $H_2O$ ), the number of possible reactants is quite manageable:



Equilibrium is quickly reached between these eight species and has been simulated for conventional, parallel-illumination, TEM geometry.<sup>56</sup> To convert from the calibrated TEM flux to the energy deposited, the stopping power of the specimen is required.<sup>65</sup> These simulations predict that this will have an overall effect of reducing the pH of water.<sup>56</sup> For the electron fluxes used in these experiments, water with initial pH 7.0 acidifies to between pH 5.1 at  $0.8 \text{ e}^- \text{ \AA}^{-2} \text{ s}^{-1}$  and pH 4.5 at  $24.8 \text{ e}^- \text{ \AA}^{-2} \text{ s}^{-1}$ . If well calibrated, the electron beam can be an electrochemical stimulus to study relevant oxidation-reduction systems.<sup>49–55</sup> Acidification caused by the reductive potential of the electron dose in liquids is analogous to some reactive environmental and biological conditions. With a properly formulated solution, this approach enables direct nanoscale observation of systems of biological, environmental, and technological significance.

The behavior of IONPs in the STEM liquid cell depends on the surface coating. If we presume an acidic pH in the TEM liquid cell, reduction and dissolution of IONPs is thermodynamically favorable except when other species or surface coatings alter the solution chemistry. Following dissolution of the primary particle, iron ions in solution may then bind electrostatically or chemically with amino acid functional groups in the coating or recrystallize as solid hydrous iron oxide depending on local chemistry and pH changes in solution. Functionalization of the  $Fe_3O_4$  surface with L-cysteine gives reversible growth and dissolution reactions, which is specific to the local changes in pH and can be controlled with the electron flux density. Metal cations, here iron, interact with amino acids altering their protonation state and in some cases forming complexes.<sup>28,66,67</sup> In particular, oxidation of cysteine by iron, and formation

of iron-cysteine complexes has been demonstrated, at least in the case of free thiol cysteine.<sup>68,69</sup> Reactivity of thioester cysteines in the coating is not necessarily the same, but we expect that iron-cysteine bonds will still form. The cysteine groups on the functionalized IONP surface serve as attachment sites for  $\text{Fe}^{2+}$  or  $\text{Fe}^{3+}$  ions in solution, potentially acting as nucleation sites for growth of secondary iron phases. In the case of L-Cys-PEG coated  $\text{Fe}_3\text{O}_4$  *in situ* formation of such organo-iron complexes is reversible, as shown in **Figure 3**. In contrast, the CPP-PEG coated sample contains several arginine sites where iron can bind electrostatically or chemically. Increasing the iron concentration stabilizes solid phases. With more active sites for iron to form complexes with the organic molecules, the local iron concentration at these functional groups will be higher than the L-cysteine sample.

## Conclusions

In all cases, the behavior of individual nanoparticles and assemblies diverge from that of bulk solution. The zeta potential in particular is not representative of behavior observed at the relevant length scales. Some particles dissolve while others grow, even within the same sample. The nanoparticle stability and reversibility of growth and dissolution reactions depend on the surface functionalization and interactions with ions in solution—local phenomena that cannot be captured in the distribution of  $\zeta$  in the sample. While the zeta potential of the functionalized nanoparticles is a primary indicator of colloidal stability, it does not account for local variations in solution composition and pH as well as reactions between metal ions, peptides, or other species. With observable behaviors at the nanoscale differing significantly from the overall sample stability, it is clear that direct *in situ* methods at relevant length scales must be an integral part of designing nanotechnologies that interface with biological and similarly complex systems.<sup>2,38</sup>

The stability of nanoparticles in aqueous solutions is of natural significance in biomedical applications. Performance in Magnetic Particle Imaging, for example, is determined by the size, size distribution, and phase of IONPs.<sup>8,23,57</sup> *In vivo* behavior of nanoparticles is also highly dependent on surface chemistry.<sup>10,23,62</sup> Formulations that agglomerate in physiological pH will lose their performance, while particles that dissolve too quickly are similarly unacceptable. Amino acid surface modifications in particular have enormous promise for targeting or other functionality, but may also have unexpected consequences for the behavior of the materials *in vivo*.<sup>7,10,11</sup> However, nanoparticle surface chemistry and functionalization provide a platform to control interactions with solution, ions, and adjacent nanoparticles. For example, surface functionalization can be optimized for *in vivo* circulation time, or to tune dissolution kinetics in biological environments.<sup>29,62</sup> Further, behavior of peptide functionalized IONPs may model compounds in natural and biological systems, for example, the interplay between proteins such as hemoglobin or ferritin and iron oxidation, metabolism, and clearance.<sup>19,67,68,70</sup> *In situ* techniques enable direct visualization of the solid-liquid interface to observe and quantify nanoscale kinetics, as we have done here to measure IONP dissolution and growth rates. This template can be applied to evaluate a wide variety of functional materials at critical length and time scales in relevant environments.

### **Acknowledgements**

A portion of this work was supported by the Chemical Imaging Initiative, a Laboratory Directed Research and Development Program at Pacific Northwest National Laboratory (PNNL). A portion of the research was performed using the William R. Wiley Environmental Molecular Sciences Laboratory, a US Department of Energy (DOE) national scientific user facility sponsored by the DOE's Office of Biological and Environmental Research and located at PNNL. PNNL is operated by Battelle for the DOE under Contract DE-AC05-76RL01830. The nanoparticle synthesis and functionalization was also supported by the National Institutes of Health under NIH 1R01EB013689-01/NIBIB, 1R41EB013520-01, 1R42EB013520-01.

## References

1. Aksay, I. A. *et al.* Biomimetic Pathways for Assembling Inorganic Thin Films. *Science* **273**, 892–898 (1996).
2. Voitchovsky, K., Kuna, J. J., Contera, S. A., Tosatti, E. & Stellacci, F. Direct mapping of the solid–liquid adhesion energy with subnanometre resolution. *Nat. Nanotechnol.* **5**, 401–405 (2010).
3. Hufschmid, R. *et al.* Direct Visualization of Aggregate Morphology and Dynamics in a Model Soil Organic-Mineral System. *Environ. Sci. Technol. Lett.* **4**, 186–191 (2017).
4. Hulsken, B. *et al.* Real-time single-molecule imaging of oxidation catalysis at a liquid–solid interface. *Nat. Nanotechnol.* **2**, 285–289 (2007).
5. Shrestha, B. R., Baimpos, T., Raman, S. & Valtiner, M. Angstrom-Resolved Real-Time Dissection of Electrochemically Active Noble Metal Interfaces. *ACS Nano* **8**, 5979–5987 (2014).
6. Prabhakaran, V. *et al.* Rational design of efficient electrode–electrolyte interfaces for solid-state energy storage using ion soft landing. *Nat. Commun.* **7**, 11399 (2016).
7. Nel, A. E. *et al.* Understanding biophysicochemical interactions at the nano–bio interface. *Nat. Mater.* **8**, 543–557 (2009).
8. Krishnan, K. M. Biomedical Nanomagnetism: A Spin Through Possibilities in Imaging, Diagnostics, and Therapy. *IEEE Trans. Magn.* **46**, 2523–2558 (2010).
9. Krishnan, K. M. Chapter 12: Magnetic Materials in Medicine and Biology. in *Fundamentals and Applications of Magnetic Materials* (Oxford University Press, Oxford, United Kingdom, 2016).

10. Pelaz, B. *et al.* Interfacing engineered nanoparticles with biological systems: anticipating adverse nano–bio interactions. *Small* **9**, 1573–1584 (2013).
11. Rivera-Gil, P. *et al.* The Challenge To Relate the Physicochemical Properties of Colloidal Nanoparticles to Their Cytotoxicity. *Acc. Chem. Res.* **46**, 743–749 (2013).
12. Kolosnjaj-Tabi, J. *et al.* The One Year Fate of Iron Oxide Coated Gold Nanoparticles in Mice. *ACS Nano* **9**, 7925–7939 (2015).
13. Feliu, N. *et al.* In vivo degeneration and the fate of inorganic nanoparticles. *Chem Soc Rev* **45**, 2440–2457 (2016).
14. Baumgartner, J. *et al.* Nucleation and growth of magnetite from solution. *Nat. Mater.* **12**, 310–314 (2013).
15. Park, J. *et al.* Ultra-large-scale syntheses of monodisperse nanocrystals. *Nat. Mater.* **3**, 891–895 (2004).
16. Perez De Berti, I. O. *et al.* Alternative low-cost approach to the synthesis of magnetic iron oxide nanoparticles by thermal decomposition of organic precursors. *Nanotechnology* **24**, 175601 (2013).
17. Arami, H., Khandhar, A., Liggitt, D. & Krishnan, K. M. In vivo delivery, pharmacokinetics, biodistribution and toxicity of iron oxide nanoparticles. *Chem Soc Rev* **44**, 8576–8607 (2015).
18. Teeman, E., Shasha, C., Evans, J. E. & Krishnan, K. M. Intracellular dynamics of superparamagnetic iron oxide nanoparticles for magnetic particle imaging. *Nanoscale* **11**, 7771–7780 (2019).
19. Weissleder, R. *al et al.* Superparamagnetic iron oxide: pharmacokinetics and toxicity. *Am. J. Roentgenol.* **152**, 167–173 (1989).

20. Arbab, A. S. *et al.* A model of lysosomal metabolism of dextran coated superparamagnetic iron oxide (SPIO) nanoparticles: implications for cellular magnetic resonance imaging. *NMR Biomed.* **18**, 383–389 (2005).
21. Levy, M. *et al.* Long term in vivo biotransformation of iron oxide nanoparticles. *Biomaterials* **32**, 3988–3999 (2011).
22. Lartigue, L. *et al.* Biodegradation of Iron Oxide Nanocubes: High-Resolution *In Situ* Monitoring. *ACS Nano* **7**, 3939–3952 (2013).
23. Arami, H. *et al.* In vivo multimodal magnetic particle imaging (MPI) with tailored magneto/optical contrast agents. *Biomaterials* **52**, 251–261 (2015).
24. López-Cruz, A., Barrera, C., Calero-DdelC, V. L. & Rinaldi, C. Water dispersible iron oxide nanoparticles coated with covalently linked chitosan. *J. Mater. Chem.* **19**, 6870 (2009).
25. Zhu, R. *et al.* Functionalization of magnetic nanoparticles with peptide dendrimers. *J. Mater. Chem.* **21**, 5464 (2011).
26. Soenen, S. J. H., Himmelreich, U., Nuytten, N. & De Cuyper, M. Cytotoxic effects of iron oxide nanoparticles and implications for safety in cell labelling. *Biomaterials* **32**, 195–205 (2011).
27. Singh, N. *et al.* The role of iron redox state in the genotoxicity of ultrafine superparamagnetic iron oxide nanoparticles. *Biomaterials* **33**, 163–170 (2012).
28. Schwaminger, S. P. *et al.* Nature of Interactions of Amino Acids with Bare Magnetite Nanoparticles. *J. Phys. Chem. C* **119**, 23032–23041 (2015).
29. Mattix, B. *et al.* Accelerated Iron Oxide Nanoparticle Degradation Mediated by Polyester Encapsulation within Cellular Spheroids. *Adv. Funct. Mater.* **24**, 800–807 (2014).

30. Gouy, G. Sur la constitution de la charge électrique à la surface d'un électrolyte. *J Phys* **9**, 457–468 (1910).
31. Chapman, D. L. LI. A contribution to the theory of electrocapillarity. *Lond. Edinb. Dublin Philos. Mag. J. Sci.* **25**, 475–481 (1913).
32. Stern, O. Zur theorie der elektrolytischen doppelschicht. *Z. Für Elektrochem. Angew. Phys. Chem.* **30**, 508–516 (1924).
33. Elbourne, A. *et al.* Nanostructure of the Ionic Liquid–Graphite Stern Layer. *ACS Nano* **9**, 7608–7620 (2015).
34. Pounds, M., Tazi, S., Salanne, M. & Madden, P. A. Ion adsorption at a metallic electrode: an *ab initio* based simulation study. *J. Phys. Condens. Matter* **21**, 424109 (2009).
35. Black, J. M. *et al.* Bias-Dependent Molecular-Level Structure of Electrical Double Layer in Ionic Liquid on Graphite. *Nano Lett.* **13**, 5954–5960 (2013).
36. Welch, D. A. *et al.* Understanding the Role of Solvation Forces on the Preferential Attachment of Nanoparticles in Liquid. *ACS Nano* **10**, 181–187 (2016).
37. Tian, P. Molecular dynamics simulations of nanoparticles. *Annu. Rep. Sect. C Phys. Chem.* **104**, 142 (2008).
38. Siretanu, I. *et al.* Direct observation of ionic structure at solid-liquid interfaces: a deep look into the Stern Layer. *Sci. Rep.* **4**, (2014).
39. LaGrange, T. *et al.* Nanosecond time-resolved investigations using the in situ of dynamic transmission electron microscope (DTEM). *Ultramicroscopy* **108**, 1441–1449 (2008).
40. Stach, E. A. Real-time observations with electron microscopy. *Mater. Today* **11**, 50–58 (2008).

41. Williamson, M. J., Tromp, R. M., Vereecken, P. M., Hull, R. & Ross, F. M. Dynamic microscopy of nanoscale cluster growth at the solid–liquid interface. *Nat. Mater.* **2**, 532–536 (2003).
42. de Jonge, N. & Ross, F. M. Electron microscopy of specimens in liquid. *Nat. Nanotechnol.* **6**, 695–704 (2011).
43. Grogan, J. M., Rotkina, L. & Bau, H. H. In situ liquid-cell electron microscopy of colloid aggregation and growth dynamics. *Phys. Rev. E* **83**, (2011).
44. Abellan, P. *et al.* Factors influencing quantitative liquid (scanning) transmission electron microscopy. *Chem. Commun.* **50**, 4873 (2014).
45. Boyes, E. D. & Gai, P. L. Environmental high resolution electron microscopy and applications to chemical science. *Ultramicroscopy* **67**, 219–232 (1997).
46. Creemer, J. F. *et al.* Atomic-scale electron microscopy at ambient pressure. *Ultramicroscopy* **108**, 993–998 (2008).
47. Chen, C. Q., Pei, Y. T. & De Hosson, J. T. M. Effects of size on the mechanical response of metallic glasses investigated through in situ TEM bending and compression experiments. *Acta Mater.* **58**, 189–200 (2010).
48. Ruska, von E. Beitrag zur übermikroskopischen Abbildung bei höheren Drucken. *Kolloid-Z.* **100**, 212–219 (1942).
49. Zheng, H. *et al.* Observation of Single Colloidal Platinum Nanocrystal Growth Trajectories. *Science* **324**, 1309–13012 (2009).
50. Woehl, T. J., Evans, J. E., Arslan, I., Ristenpart, W. D. & Browning, N. D. Direct *in Situ* Determination of the Mechanisms Controlling Nanoparticle Nucleation and Growth. *ACS Nano* **6**, 8599–8610 (2012).

51. Parent, L. R. *et al.* Direct *in Situ* Observation of Nanoparticle Synthesis in a Liquid Crystal Surfactant Template. *ACS Nano* **6**, 3589–3596 (2012).
52. Hermannsdörfer, J., de Jonge, N. & Verch, A. Electron beam induced chemistry of gold nanoparticles in saline solution. *Chem Commun* **51**, 16393–16396 (2015).
53. Huang, J. Y. *et al.* In Situ Observation of the Electrochemical Lithiation of a Single SnO<sub>2</sub> Nanowire Electrode. *Science* **330**, 1515–1520 (2010).
54. Mehdi, B. L. *et al.* Observation and Quantification of Nanoscale Processes in Lithium Batteries by Operando Electrochemical (S)TEM. *Nano Lett.* **15**, 2168–2173 (2015).
55. Gu, M. *et al.* In Situ TEM Study of Lithiation Behavior of Silicon Nanoparticles Attached to and Embedded in a Carbon Matrix. *ACS Nano* **6**, 8439–8447 (2012).
56. Schneider, N. M. *et al.* Electron–Water Interactions and Implications for Liquid Cell Electron Microscopy. *J. Phys. Chem. C* **118**, 22373–22382 (2014).
57. Hufschmid, R. *et al.* Synthesis of phase-pure and monodisperse iron oxide nanoparticles by thermal decomposition. *Nanoscale* **7**, 11142–11154 (2015).
58. Kemp, S. J., Ferguson, R. M., Khandhar, A. P. & Krishnan, K. M. Monodisperse magnetite nanoparticles with nearly ideal saturation magnetization. *RSC Adv* **6**, 77452–77464 (2016).
59. Gonzales, M. & Krishnan, K. M. Phase transfer of highly monodisperse iron oxide nanocrystals with Pluronic F127 for biomedical applications. *J. Magn. Magn. Mater.* **311**, 59–62 (2007).
60. Yu, W. W., Chang, E., Sayes, C. M., Drezek, R. & Colvin, V. L. Aqueous dispersion of monodisperse magnetic iron oxide nanocrystals through phase transfer. *Nanotechnology* **17**, 4483–4487 (2006).

61. Pennycook, S. J. Z-contrast STEM for materials science. *Ultramicroscopy* **30**, 58–69 (1989).
62. Khandhar, A. P., Ferguson, R. M., Arami, H., Kemp, S. J. & Krishnan, K. M. Tuning surface coatings of optimized magnetite nanoparticle tracers for in vivo Magnetic Particle Imaging. *IEEE Trans. Magn.* **51**,
63. Chantrell, R. W., Popplewell, J. & Charles, S. W. Measurements of Particle Size Distribution Parameters in Ferrofluids. *IEEE Trans. Mag.* **MAG-14**, 975–977 (1978).
64. Browning, N. D., Chisholm, M. F. & Pennycook, S. J. Atomic-resolution chemical analysis using a scanning transmission electron microscope. *Nature* **366**, 143–146 (1993).
65. Berger, M. J., Coursey, J. S., Zucker, M. A. & Chang, J. Stopping-Power & Range Tables for Electrons, Protons, and Helium Ions. *NIST Stand. Ref. Database* **124**, (2017).
66. Dudev, T. & Lim, C. Factors Governing the Protonation State of Cysteines in Proteins: An Ab Initio/CDM Study. *J. Am. Chem. Soc.* **124**, 6759–6766 (2002).
67. Bottari, E., Festa, M. R. & Gentile, L. An Investigation on the Equilibria between Arginine and Iron(II) and Iron(III). *J. Chem. Eng. Data* **58**, 718–723 (2013).
68. Neville, R. G. The oxidation of cysteine by iron and hydrogen peroxide. *J. Am. Chem. Soc.* **79**, 2456–2457 (1957).
69. Michaelis, L. & Barron, E. G. Oxidation-Reduction Systems of Biological Significance IV. Comparative Study of the Complexes of Cysteine with the Metals of the Iron Group. *J. Biol. Chem.* **83**, 191–210 (1929).
70. Wang, C., Qiao, Q., Shokuhfar, T. & Klie, R. F. High-Resolution Electron Microscopy and Spectroscopy of Ferritin in Biocompatible Graphene Liquid Cells and Graphene Sandwiches. *Adv. Mater.* **26**, 3410–3414 (2014).



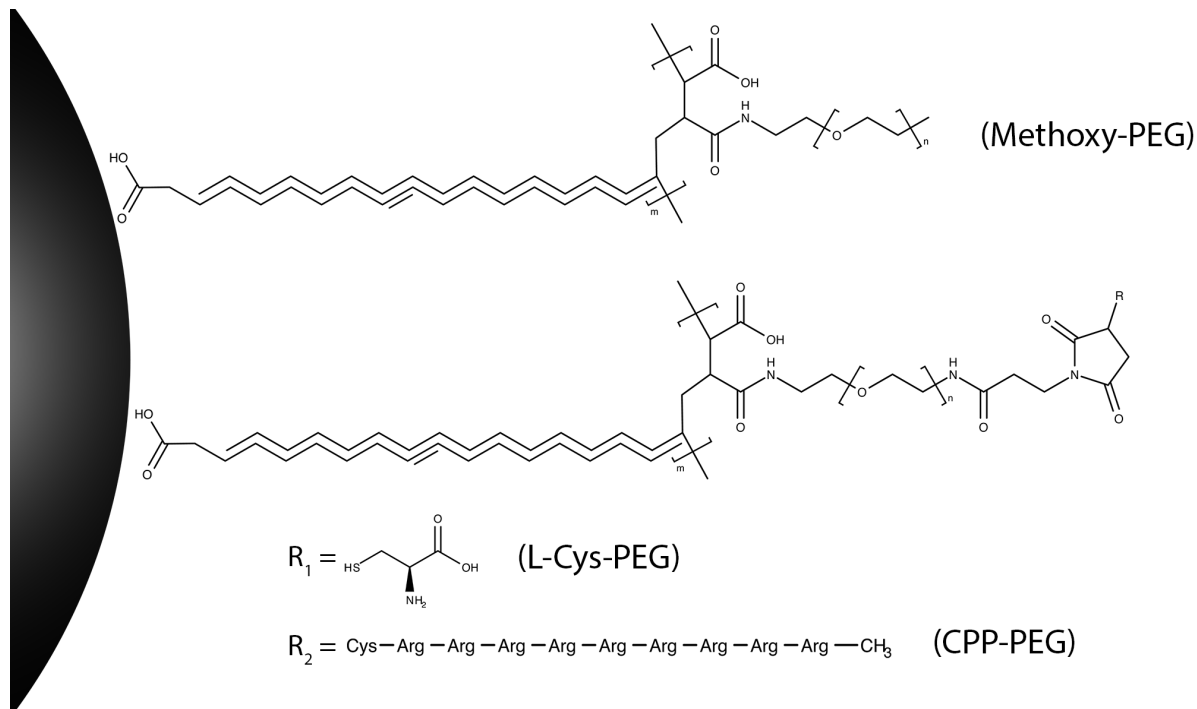


**Figure 1** Schematic of the nanoparticle coating. Monodisperse superparamagnetic iron oxide nanoparticle cores with diameter,  $d_C$ , are coated with PMAO-PEG increasing the hydrodynamic size,  $d_H$ . PEG terminated nanoparticles may be functionalized, L-cysteine shown, which changes surface properties such as the zeta potential,  $\zeta$ .

**Table 1** Physio-chemical properties of the iron oxide nanoparticle samples. Core diameter ( $d_C$ ) and log-normal size distribution,  $\sigma$ , are fit to VSM data and confirmed with TEM ( $n = 5216$  particles). Hydrodynamic diameter ( $d_H$ ) and zeta potential ( $\zeta$ ) are measured by DLS in DI water. STEM stability summarizes the critical electron flux values that changed colloidal stability in these experiments.

$d_C$ [nm]	$\sigma$ log-normal		$d_H$ [nm]	$\zeta$ [mV]	Liquid STEM Stability
27.2 (VSM)	0.05 (VSM)	$Fe_3O_4@$ <i>Methoxy-PEG</i>	90	-7	Stable $< 0.8 e^- \text{ \AA}^{-2} s^{-1}$ Dissolves $\geq 0.8 e^- \text{ \AA}^{-2} s^{-1}$
		$Fe_3O_4@$ <i>CPP-PEG</i>	77	23	Stable $< 1.3 e^- \text{ \AA}^{-2} s^{-1}$ Growth $\geq 1.3 e^- \text{ \AA}^{-2} s^{-1}$ Dissolves $\geq 14.1 e^- \text{ \AA}^{-2} s^{-1}$
27.7 (TEM)	0.06 (TEM)	$Fe_3O_4@$ <i>L-Cys-PEG</i>	70	-40	Stable $< 1 e^- \text{ \AA}^{-2} s^{-1}$ Growth $\geq 5.2 e^- \text{ \AA}^{-2} s^{-1}$ Re-dissolves $\geq 1.8 e^- \text{ \AA}^{-2} s^{-1}$

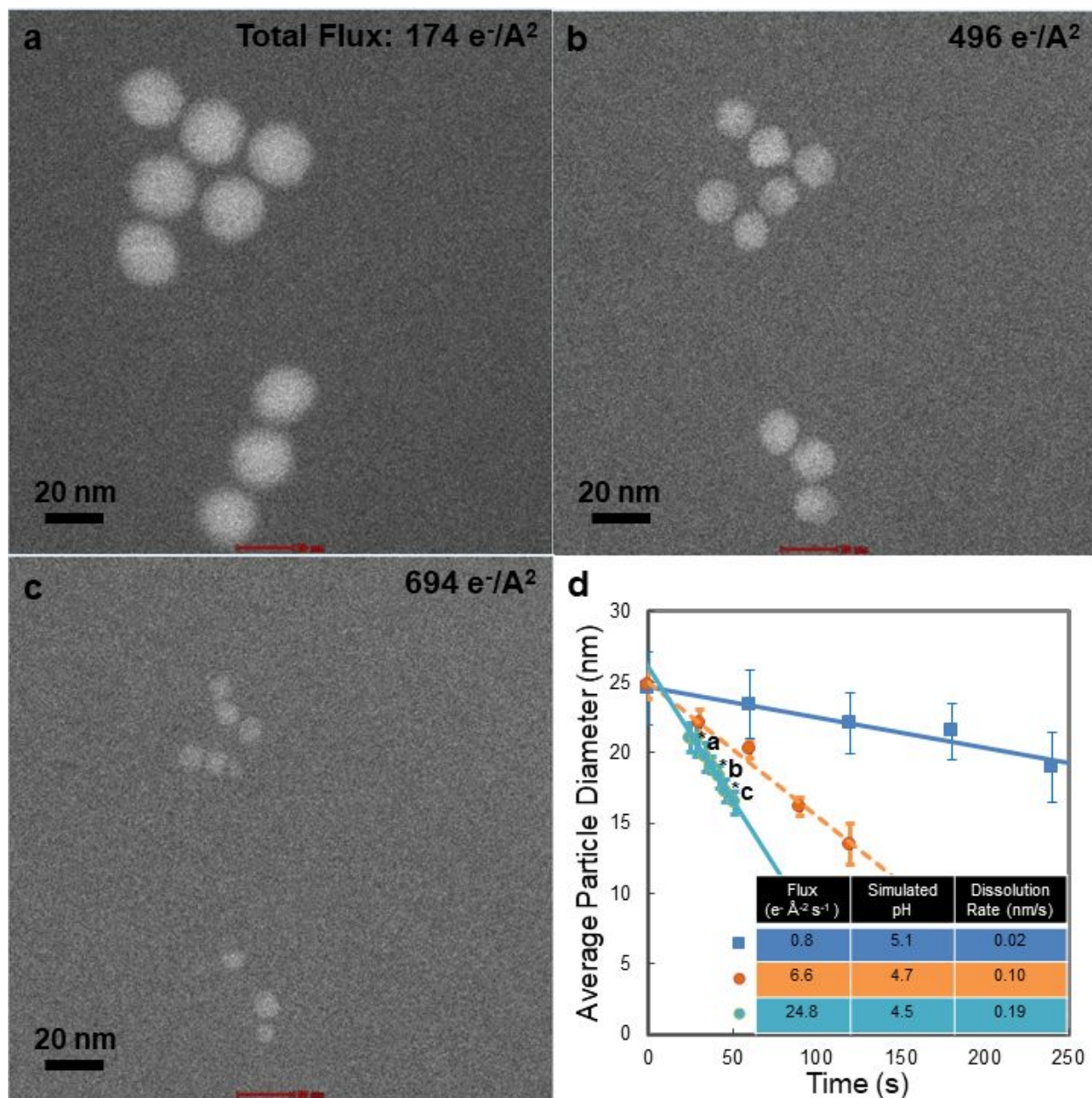


**Figure 2** Magnetite nanoparticles terminated with PEG dissolve in water during electron irradiation. This is dependent on total dose. (a)-(c) are movie frames (total electron dose noted) throughout dissolution at  $24.8 \text{ e}^- \text{\AA}^{-2} \text{s}^{-1}$ , (d) plot showing decrease in average particle size versus accumulated electron dose. The steady state pH is estimated for a thin film of water, starting at pH 7 and subjected to the respective electron flux density, using published code.<sup>56</sup>

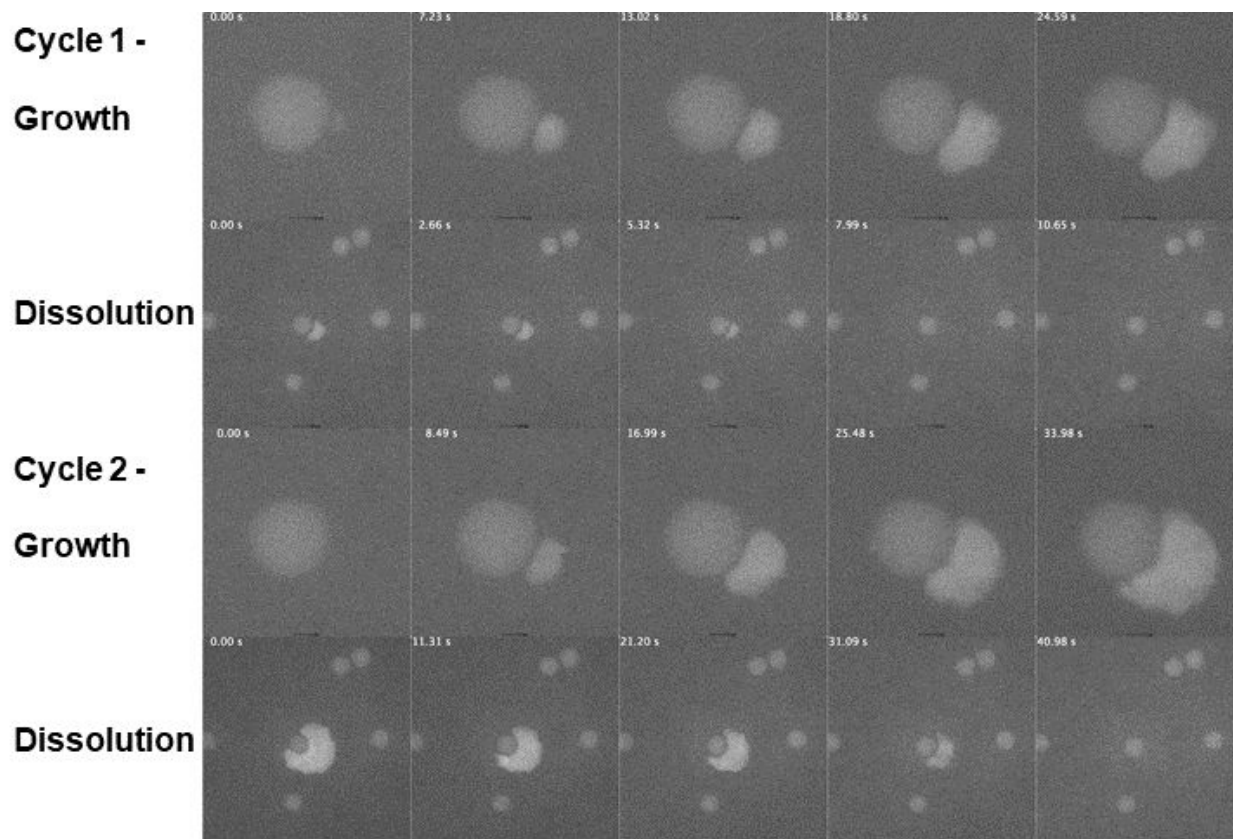


**Figure 3** Growth at the surface of L-cysteine functionalized nanoparticle is reversed by reducing magnification and electron flux density. At higher flux density, here  $5.2 \text{ e}^- \text{ \AA}^{-2} \text{ s}^{-1}$ , ions accumulate at the particle surface forming an amorphous iron-rich phase. When the flux density is reduced to  $1.8 \text{ e}^- \text{ \AA}^{-2} \text{ s}^{-1}$  iron dissolves back into solution. See Supplemental Movie 2.

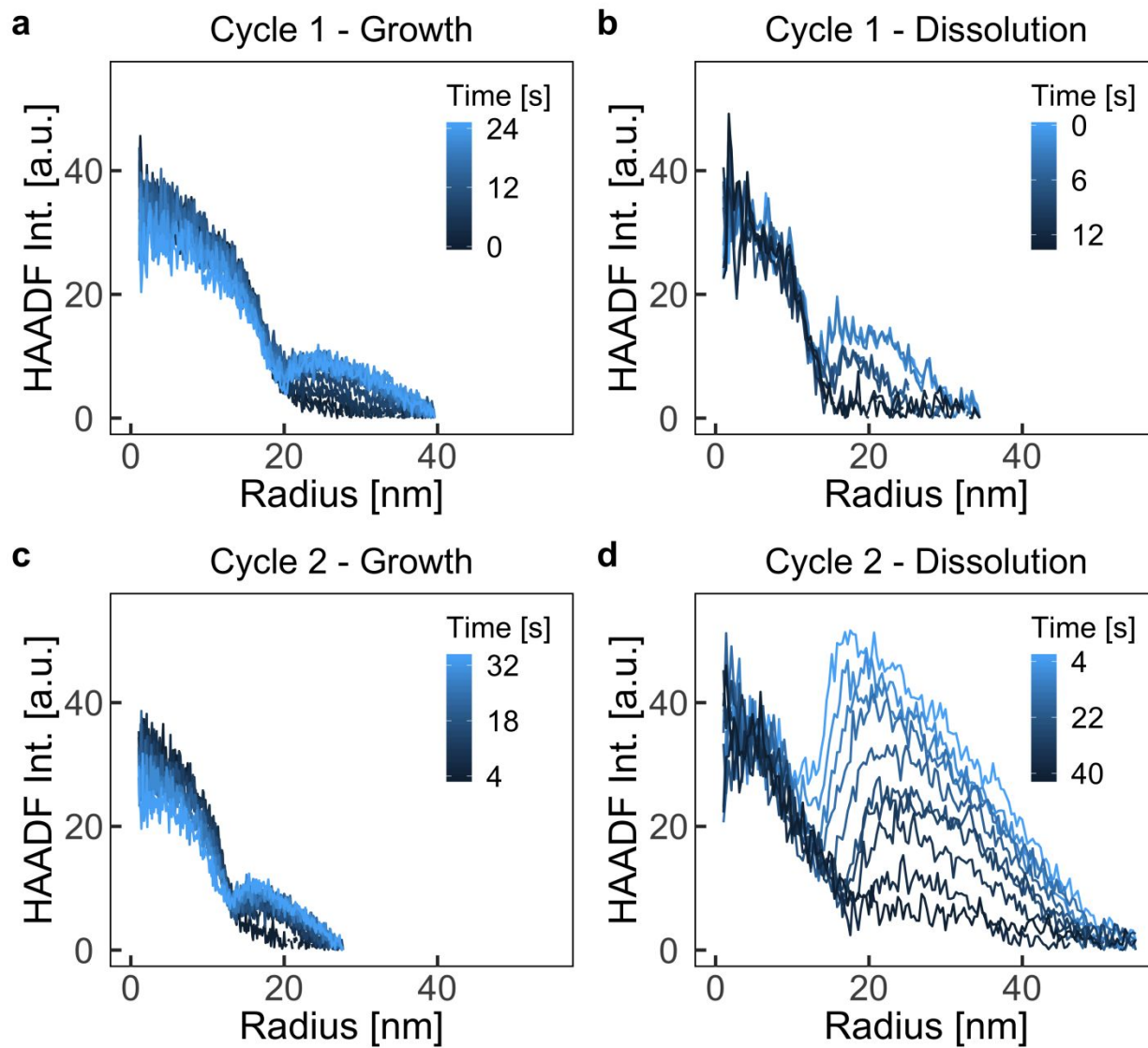


**Figure 4** The radially integrated HAADF intensity indicates the distribution of iron throughout the experiment shown in figure 3 and Supplemental Movie 2. From this, the average velocity of the interface is measured to be  $0.4 \text{ nm s}^{-1}$  for the growth, and  $-0.2 \text{ nm s}^{-1}$  for the dissolution.

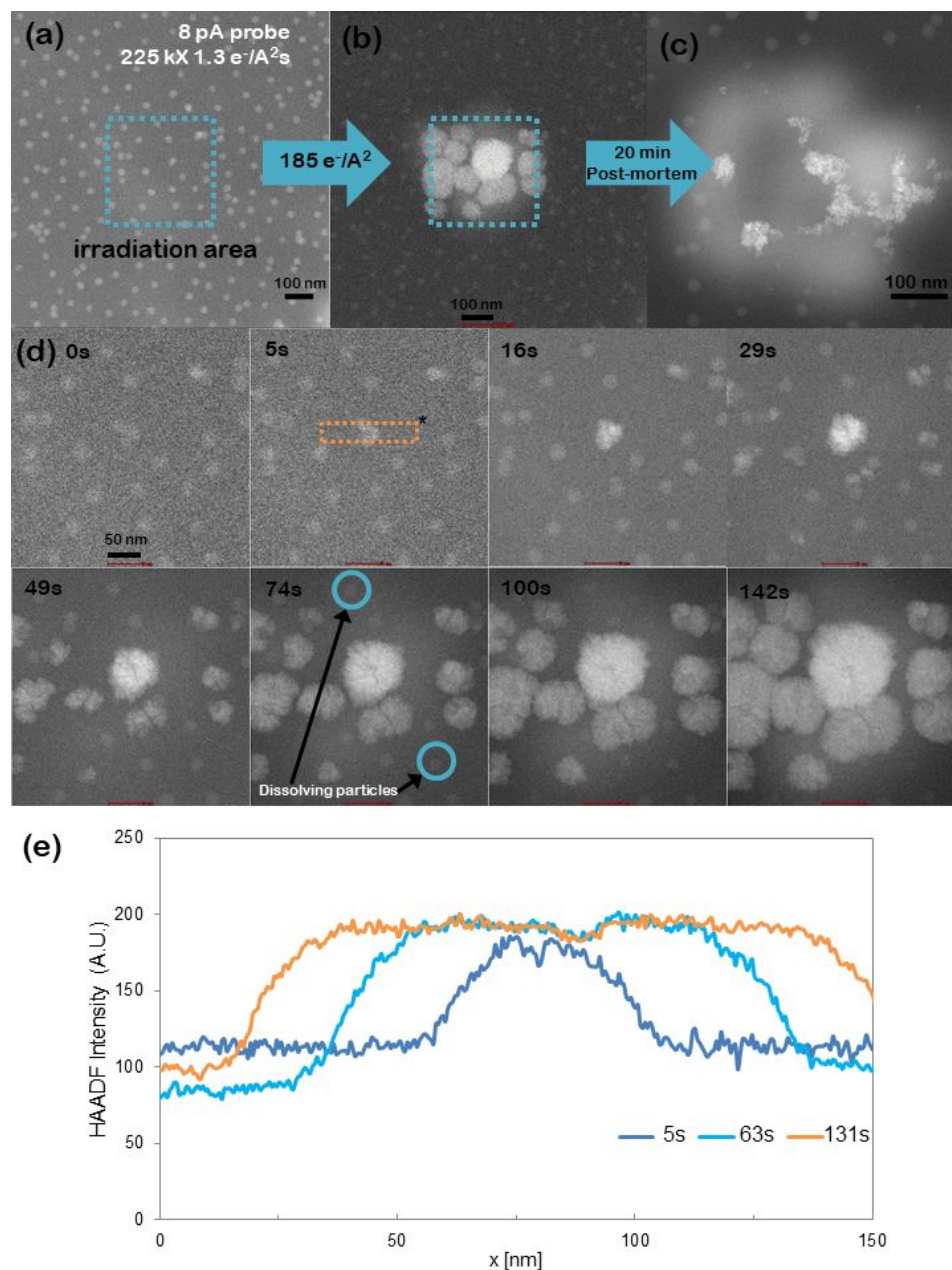


**Figure 5** For this ensemble of magnetite nanoparticles functionalized with poly-cationic peptide (CPP-PEG) iron growth at the particle surface (**b**, and time series **d**) follows dissolution of the primary  $\text{Fe}_3\text{O}_4$  nanoparticles. Dissolving particles are circled in the time series. Dashed rectangle\* indicates integration window for (**e**). When the beam is removed, densification and recrystallization as a disordered, mixed-valence, hydrated iron oxide phase occurs over approximately 20 min (**c**).